ARTICLE

Solar-driven plasmonic heterostructure Ti/TiO_{2-x} with gradient doping for sustainable plasmon-enhanced catalysis

Received 00th January 20xx,
Accepted 00th January 20xx

DOI: 10.1039/x0xx00000x

Chaoqun Cheng,[a] Muhammad Nadeem Akram,[a] Ola Nilsen,[b] Nini Pryds [c] and Kaiying Wang*[a]

Plasmon-enhanced harvesting of photons has contributed to the photochemical conversion and storage of solar energy. However, high dependence on noble metals and weak coupling in heterostructures constrains the progress towards sustainable plasmonic enhancement. Here earth-abundant Ti is studied to achieve plasmonic enhancement of catalytic activity in a solar-driven heterostructure of Ti/TiO_{2-x}. The heterostructure was fabricated by engineering an intense coupling of surface-etched Ti metal and gradient-based TiO_{2-x} dielectric via diffusion doping. The Ti/TiO_{2-x} allows a highly resonant light absorption band associated with surface plasmon resonances that exhibit strong near-field enhancement (NFE) and hot electron injection effects. In photoelectrochemical system, intense interaction of the resonant plasmons with vicinity TiO_{2-x} dielectric accelerates the transfer of solar energy to charge carriers for plasmon-enhanced water splitting reactions. Moreover, the plasmonic Ti/TiO_{2-x} presents sustained enhanced redox activities over 100 h. The intense coupling by gradient doping offers an effective approach to enable the plasmon resonances of Ti excited by visible light. The Ti-based plasmonic heterostructure potentially opens an alternative avenue towards sustainable plasmon-enhanced catalysis.

Introduction

Plasmon resonances provide an exciting path to advance catalytic conversion and storage of solar to chemical energy[1-5]. The plasmons in metals (typically Au and Ag) can harvest photons from visible to infrared light by tuning their morphology[6,7]. Hetero-coupling the plasmonic metals with semiconductors as plasmonic heterostructures is widely used to enhance the absorption of solar energy to drive chemical reactions through hot carrier injection, near-field enhancement and/or light scattering effects[3,8]. However, intrinsic features of the plasmonic heterostructures limit its further development for highly efficient coupling of plasmons with solar light and yields of energetic charge carriers, such as the weak coupling[9-11], dependence on noble metals and complexity of fabrication. Nowadays, the non-noble metals have been attracting high research interests due to their abundance and superior physicochemical properties[12-15], but only few non-noble materials can support plasmon resonances (SPRs) in the visible light region and overcome the challenges which include chemical stability, controllability and reliable synthesis[12].

In principle, metal Ti interfacing with a proper dielectric environment, such as titanium oxides, can activate SPRs [16-19]. The plasmonic energy could then be transferred to the dielectric of titanium oxides for applications. Since the first successful trial of TiO_2 to split water under ultraviolet light in 1972 by Fujishima and Honda[20], a variety of strategies have been explored to enhance visible light driven catalytic activities[21], such as the plasmonic noble metals hetero-coupled with TiO_2[22]. The earth abundant Ti could function as an alternative plasmonic metal for sustainable enhancement. However, excitation of plasmon resonances of Ti in the visible light region and extraction of the plasmonic energy has not been achieved and basically studied.

Herein, gradient-based heterostructure is proposed as a promising path by engineering a metal coupled with a gradient-based dielectric. Diffusion doping[23] is employed to inject foreign atoms in the surface region of metal, forming a gradient-based dielectric intensely coupling with underneath metal. Variations of dopant stoichiometry affect the distribution of hetero-atoms and further states and density of free carriers[24]. Therefore, it is possible to manipulate the dielectric properties at the interface between metal and dielectric via the diffusion doping, enabling SPRs excited by visible light.

A gradient-based heterostructure Ti/TiO_{2-x} is fabricated via a thermal diffusion doping process[25], using non-noble metal Ti foils with micro- and/or nano- prisms on the surface created by chemical etching process. The prisms were designed to increase aspect ratio of nanostructured surface edges for high density of hot spots and provide active sites for reactions. Excitation of SPRs of Ti and transfer mechanism of the plasmonic energy to chemical molecules through the gradient dielectric were both investigated experimentally and theoretically. Our findings show that the SPRs of Ti are excited by visible light. The gradient-based heterostructure Ti/TiO_{2-x} presents a strong resonant light absorption band associated with the SPRs that exhibit both NFE and hot electrons generation effects. Intense

[a] Department of Microsystems, University of South-Eastern Norway, Raveien 215, 3184 Horten, Norway.
[b] Department of Chemistry, University of Oslo, Postboks 1033, 0315 Oslo, Norway.
[c] Department of Energy Conversion and Storage, Technical University of Denmark, Risø Campus, 4000 Roskilde, Denmark.
* Kaiying.Wang@usn.no

Electronic Supplementary Information (ESI) available: [details of any supplementary information available should be included here]. See DOI: 10.1039/x0xx00000x

interaction of SPRs between plasmonic Ti metal and gradient-based TiO_{2-x} dielectric accelerates the conversion of solar to chemical energy. After the coating of Ni thin film, the plasmonic heterostructure possess a long-term stability over 100 hours in the photoelectrochemical environment. The gradient-based heterostructure represents a novel approach to enable the SPRs of Ti excited in the visible light spectrum for sustainable plasmon-enhanced catalysis and photochemical applications.

Results and discussion

Gradient-based heterostructure Ti/TiO_{2-x}

Fig. 1a shows two steps of the fabrication process: (1) an etching process for preparing the micro- and nano- prisms on the surface of Ti foils and (2) thermal oxidation to allow diffusion of oxygen into the surface of the patterned Ti foil. Scanning electron microscopy (SEM) and white-light interferometer were employed to examine the surface micro- and nano- prisms array (Fig. 1b-I, II). After the etching, SEM images show a high-density of micro- and nano- prisms formed on the surface (Fig. 1b I). The diameter of quasi-particles on the surface is about 10 nm (Fig. 1b II). After thermal oxidation, the micro- and nano- prisms pattern remained the same (Fig. 1b III) with height in range of 0.0 - 2.0 µm. The morphology of micro-prisms was further examined by atomic force microscopy (AFM) surface topology (Fig. S1). The etched Ti foils with prisms (before the thermal oxidation) are referred as Ti foil in following text.

Energy-dispersive X-ray (EDX) element analysis shows that Ti and O are distributed homogeneously on the top-surface with atomic ratio close to 1:2 (Fig. 2, a and b), forming a thin-film dielectric of TiO_2 on the top surface. A dedicated line-scan EDX along the cross-section from the top into deep surface layer discloses that the oxygen content gradually decreases from the top surface to the inner space, while the Ti content shows opposite tendency. The oxygen concentration shows a decreasing amount down to about distribution around 500 nm underneath the top surface. The cross-section revealed the formation of a varied-stoichiometry of titanium oxides from the top TiO_2 dielectric thin film on the surface via a transition region TiO_{2-x} ($0 < x < 2$) to underlying pure Ti in the bulk[25]. This profile forms a quasi-sandwich configuration of the top dielectric film, middle transition region, and bottom original metal[26]. Gradient variation of the dopant in the transition region constructs heterogeneous junctions. X-ray diffraction pattern taken from these samples shows broadened peaks of Ti and rutile TiO_2 phases (Fig. S2), indicating the presence of a transition-phase state of amorphous/crystalline. The Gradient-based transition-phase state agrees with the possible formations of Ti and O with various formations, noted as TiO_{2-x} ($0 \le x \le 2$). The variation affects stoichiometry of hetero-atoms and therefore states and density of free charge carriers, benefiting the transition region with a favoured variety of dielectric constant. For example, mixed-phase titanium oxides[27] and vacancies[28] of O and Ti can be specially formed to create proper interfacing between TiO_2 dielectric and Ti metal.

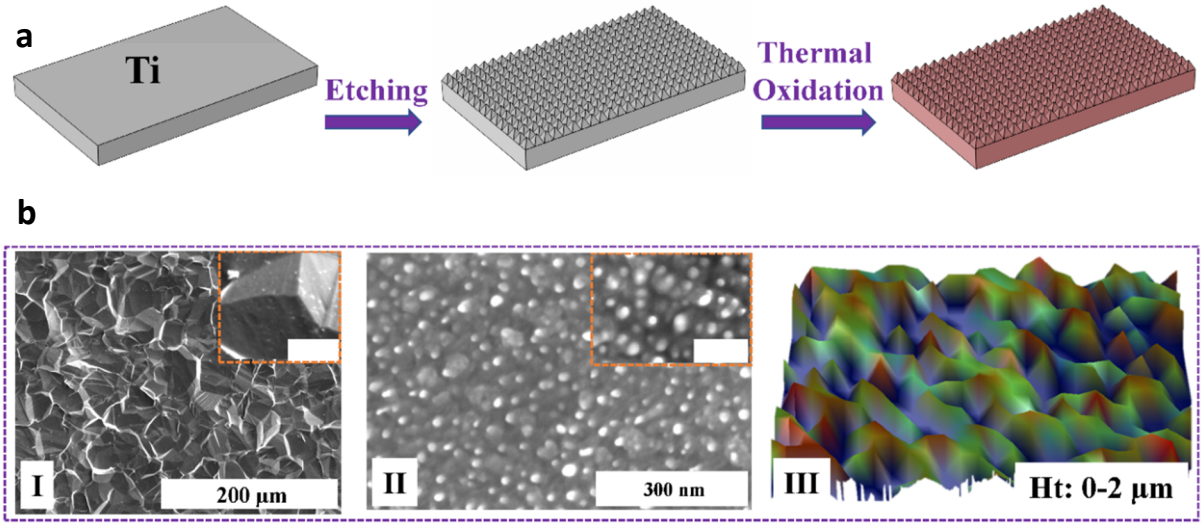

Fig. 1. Fabrication and micro/nano- prisms on a Ti/TiO_{2-x}. (a) Scheme for the processes: first etching to prepare micro- and nano- prisms on the surface of Ti foil and subsequent thermal diffusion of oxygen into the surface. (b) Scanning electron microscopic top views: surface prisms (I) (the insert scale bar, 6 µm) and surface nanoparticles (II) (the insert scale bar, 100 nm). 3-dimensional mapping (III) of the surface micro- and nano- prisms scanned by an interferometer. The height of the prisms is in the range of 0.0 - 2.0 µm.

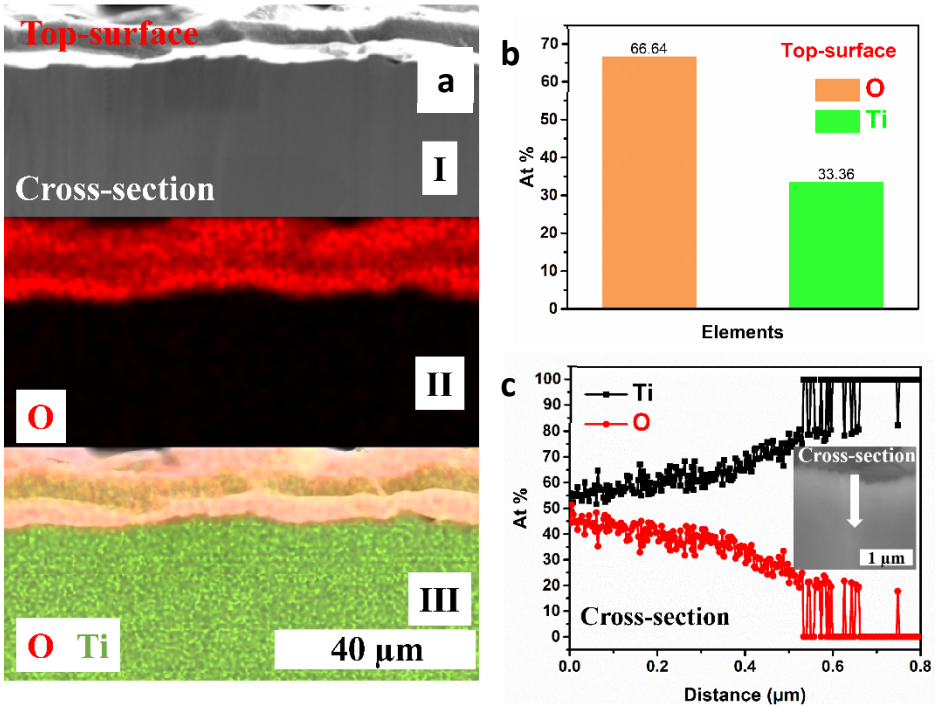

Fig. 2. Energy dispersive X-ray spectrometry analysis. (a) SEM of the cross-section. Image (**I**); mapping of oxygen (O, red) element (**II**); and mapping of mixed O (red) and Ti (green) elements (**III**). (b) Composition of O and Ti on the top surface. c) Composition of Ti and O along the cross-section. The insert is the scanning direction from the top edge into internal surface region. Scale bar: 1 µm.

Optical properties

Fig. 3a shows the absorption spectra for bulk Ti foil and Ti/TiO_{2-x}. Both spectra show a basic spectrum valley at around 350 nm. Remarkably, the Ti/TiO_{2-x} has a strong resonant absorption peak in the visible light range. According to the K-M function, the quality factor of the resonant absorption band is estimated to be about 8 which is close to the value of ~9 for gold nanoparticles[24]. This factor is defined by the ratio of the resonant peak energy to the FWHM (Full width at half maximum) energy. For both specimens, absorption with small amplitude in the ultra-violet light range is assigned to an intrinsic absorption of TiO_2 due to the native oxidation layer on Ti and the TiO_2 on the surface of Ti/TiO_{2-x}[26]. Fig. 3b shows a dark field image of Ti/TiO_{2-x} exhibiting a distinct glowing on the surface due to scattering and free-space decaying on the peripheral[29]. This was not observed in the Ti foil (Fig. S3, a-c). The orange-yellow glowing color is consistent with the light wavelength of the absorption peak, indicating the possible excitation of plasmon resonances. Moreover, the resonant absorption band is even repeatable and controllable with a regular red-shifting by variation of oxidation time (Fig. S4). The redshift is due to alteration of the dielectric properties, such as thickness and optical constant, resulting in the transformation of electromagnetic field interaction between the dielectric and the metal substrate. The results are strongly related to the excitation of SPRs due to appropriate momentum of dielectric couples of photons into the surface plasmon of Ti metal substrate, ruling out the possibility that the absorption peak is induced by defects associated with oxygen vacancies[30].

In general, the refractive index of the surrounding medium has an impact on the intensity and position of plasmon-induced light absorption peaks[31]. The Ti/TiO_{2-x} was immersed in different solvents, air, 0.5 M Na_2SO_4 and 1 M NaOH aqueous solutions with refractive indices of 1, 1.3338 and 1.3358, respectively. Fig. 3c shows the absorption spectra of Ti/TiO_{2-x} under the influence of different solvents. The absorption band shows a blue shift with increasing the refractive index, as expected from the characteristic of resonant plasmons[32]. The reversible blueshift could be explained by a negative charging in the solution, thereby causing a change of charge carrier density in surface dielectric[33].

To further explore plasmon resonances in the Ti/TiO_{2-x} and relevance of the resonant light absorption band with surface plasmons, we have employed finite-element-method based calculations in the frequency-domain to extract the spatial electric field distribution in an approximated 3-dimensional model (Fig. S5). The spatial field distribution (Fig. 3d, Fig. S6-S10) shows the maximum of electric field enhancement that is localized in the region between TiO_2 nanoparticle and Ti following the trend of respective wavelengths, due to the polarization of surface plasmons in the Ti metal substrate with the presence of TiO_2 on the top[34]. The electric field enhancement spectra disclose two distinctive enhancement bands (Fig. 3e and 3f). One is at around 290 nm, and the other is at about 430 nm. The enhanced bands in the gap is dominated closing to the bottom surface of TiO_2 particle, becoming more pronounced when gradient decreasing the thickness of TiO_2 dielectric film. In contrast, enhanced field band is becoming

more pronounced in the interface between the Ti metal and TiO_2 film dielectric (Fig. S6-S10), when gradient increasing the thickness of TiO_2 dielectric film in the gap. The enhanced field distribution verifies that the surface dielectric particles promote the excitation of localized surface plasmonic resonances (LSPRs) by coupling light into the metal, while gradient increasing the thickness of TiO_2 film in the gap enables a confined excitation of SPRs in the interface between the dielectric and the metal substrate. Hybrid coupling of both excitations results in enhanced resonant light absorption band in the visible light range (Fig. 3e and 3f).

The absorption valley at around 350 nm and the peak band close to 450 nm in the absorption enhancement spectra (Fig. 3e and 3f) both correlate with the field enhancement bands. In addition, the absorption peaks in the absorption enhancement spectra show a slight red shifting with a gradient increasing the thickness of TiO_2 dielectric film, corresponding with the red shifting of the experimental resonant absorption peaks. With adjustment of the parameters, the calculated absorption band agrees with the positions of resonant absorption peaks obtained in the experimental absorption spectra. The calculated results further support the excitations of SPPs and LSPRs in the Ti/TiO_{2-x}. The resonant plasmons exhibit strong near-field effect interacting with surface mass through the transition region between Ti metal and gradient-based dielectric for applications.

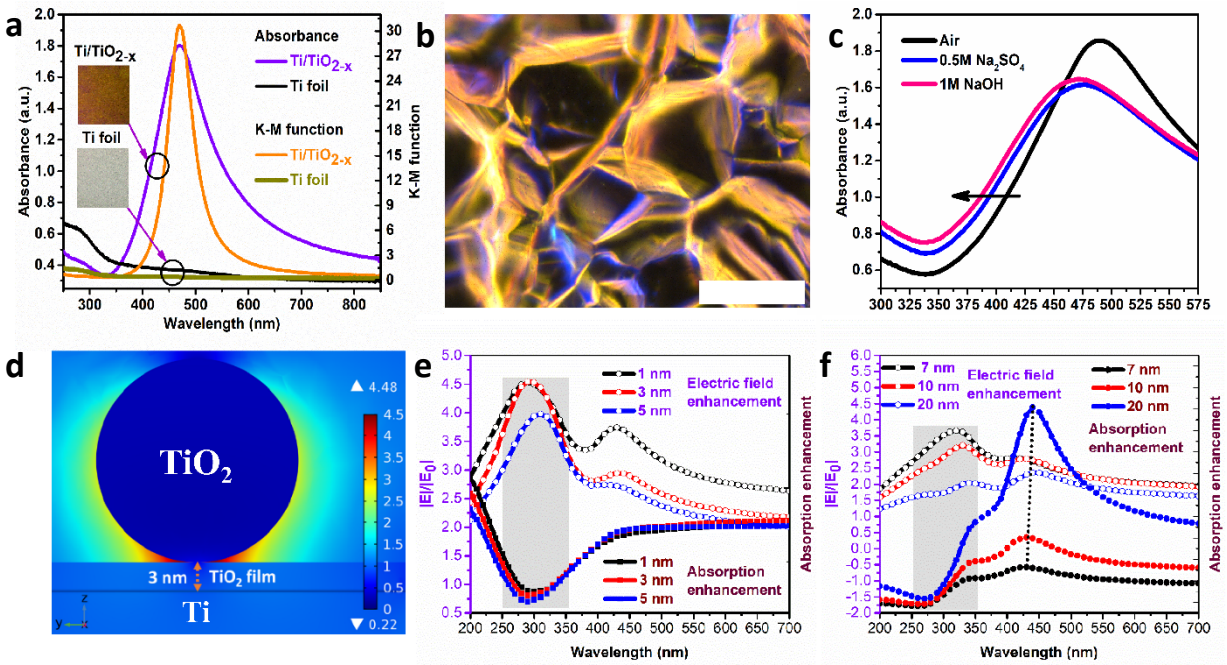

Fig. 3. Plasmon-induced solar-light absorption and near-field enhancement in a Ti/TiO_{2-x} upon excitation. (a) Strong optical absorption of representative Ti/TiO_{2-x} with a high absorption-to-scattering ratio (K-M function), compared with that of etched Ti foil. (b) Dark-field optical scattering image of the Ti/TiO_{2-x} (scale bar: 25 μm). (c) The Ti/TiO_{2-x} immersed in three different dielectrics: Air without a solution, 0.5 M Na_2SO_4 and 1M NaOH aqueous solutions, with refractive indices of 1, 1.3338 and 1.3358, respectively. (d) Spatial field-enhancement distribution $|E|/|E_0|$ at 290 nm for a nanoparticle of TiO_2 placed over a Ti substrate, with a 3 nm TiO_2 film filled in the gap. (e) At a varied thickness of 1, 3 and 5 nm of TiO_2 dielectric film, spectral maximum of the field intensity-enhancement in the gap (**Left**), and corresponding light absorption enhancement (**Right**). (f) Same as (e) but with an altered thickness of 7, 10 and 20 nm TiO_2 dielectric film.

Plasmon-enhanced photoactivities for photoelectrochemical application.

To investigate the effect of resonant plasmons on the energy transformation in Ti/TiO_{2-x}, a photoelectrochemical system was employed, in which the Ti/TiO_{2-x} was used as a working electrode. The Ti/TiO_{2-x} immersed into liquid electrolyte forms close and firm contacting interface. The built-in potential was characterized by open-circuit potential (V_{oc}) under simulated solar light illumination (Fig. 4a). Saturation potential in the V_{oc} corresponds to a steady-state distribution of the carriers. A large numerical difference between the V_{oc} under the illumination and in the dark, Δ_{Voc} = -350 mV, clearly indicates that the polarizability of electron and hole carriers upon excitation has been maintained, while back-recombination processes are retarded dramatically[35-37]. In KOH solution, the positive carriers move towards electrode/electrolyte interface, while the negative carriers move to the opposite direction. The negative tangent slope in Mott-Schottky curves (Fig. S11a) reveals an n-type conductivity of the Ti/TiO_{2-x} both in the dark and under the light. Therefore, the balanced distribution of carriers in bulk shifts the V_{oc} to a more negative value upon excitation. Finally, a high plasmonic photovoltage of 350 mV is established across the heterojunction. Indeed, for example of a

p-type photoelectrode, a positive shift caused by light irradiation was observed in V_{oc}[37]. With the high plasmonic photovoltage, the Ti/TiO_{2-x} can not only generate electron-hole pairs but also obtain a large amount of separated charge carriers for photoelectron-chemical reactions[5].

Giving an appropriate thermodynamic potential, the separated charge carriers can activate photoelectrochemical reactions to generate current. The Ti/TiO_{2-x} as a photoanode shows an enhanced photocurrent that is reproducible and timely response to the periodic solar light illumination (Fig. 4b). When the light illumination is shielded, the anodic current drops immediately to a steady state without undergoing any attenuation which would be manifested by transient spikes. Spikes are usually observed due to bulk or surface recombination[35,38]. The absence of spikes indicates that the ultrafast recombination process is inhibited. The continuous current response of the chemical reaction versus sweeping potential was also evaluated by linear sweep voltammetry (Fig. 4c). Under exposure to simulated sunlight, the obtained current is amplified by a factor of 210 at a bias of 0.23 V compared to the dark. A 200-fold enhancement is also obtained in the electrolyte Na_2SO_4 (Fig. S11b). In addition, the anodic current shows a nearly linear response to different light power illumination, which is consistent with the expected OER driven by the hole carriers (Fig. S11c).

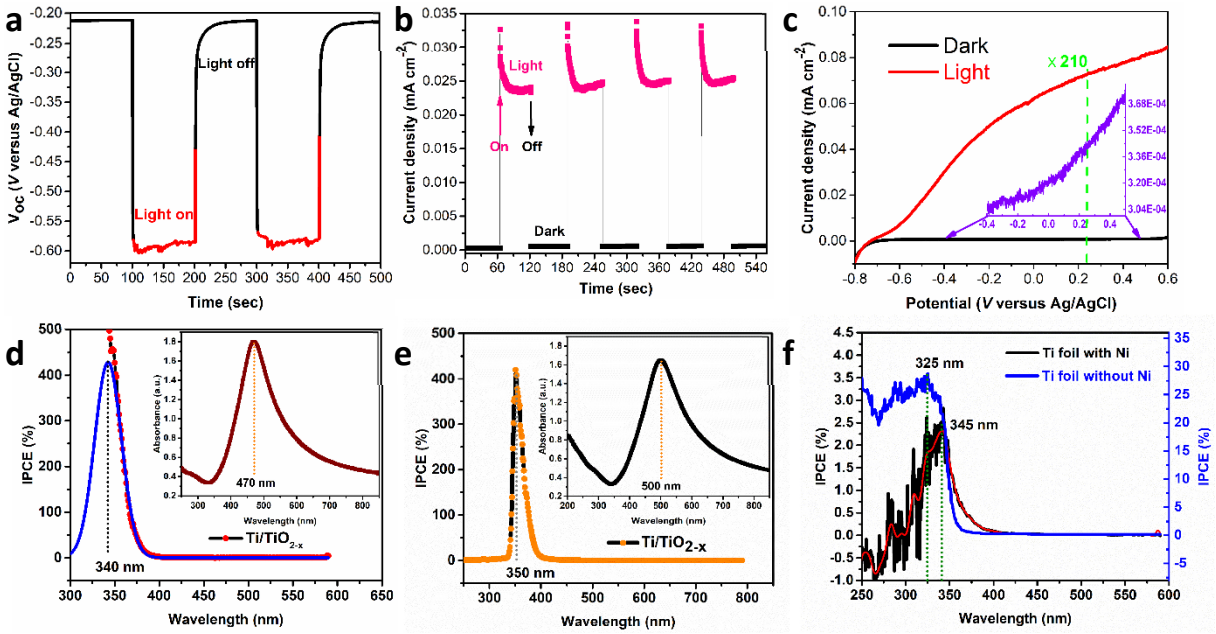

Fig. 4. Photoelectrochemical performance of the Ti/TiO_{2-x}. (a) Chronopotentiometry of open-circuit voltage (V_{oc}). The solution was quietly placed in the dark with the photoanode immersed in the electrolyte for 2 h prior to the measurement. (b) Chronoamperometry at a fixed 0 V under chopped light. (c) Linear sweep voltammetry in the dark and under the light, respectively, at 1 mV/s. (d-f) Incident photon-to-current conversion efficiency (IPCE) spectra as a function of the wavelength at a constant potential of 0.21 V vs. Ag/AgCl. (d) IPCE spectrum of the Ti/TiO_{2-x}; the peak centered at 340 nm (blue line) was determined by fitting the IPCE band to a Gaussian function. The inset is the corresponding absorbance spectra. (e) IPCE spectrum of a second specimen Ti/TiO_{2-x} with an enhancement peak centered at 350 nm. The insert is an absorbance spectrum of the second Ti/TiO_{2-x} specimen. (f) IPCE spectrum for the Ti foils before (black line and left y-axis) and after coating 2-nm Ni film followed by annealing (blue line and right y-axis), respectively.

Incident photon-to-current conversion efficiency (IPCE) spectra were measured to clarify the dependence of the OER on the solar light at a specific energy. Interestingly, an enhancement peak locates at 340 nm (blue line, Fig. 4d). The entire IPCE spectrum shows a high conversion efficiency region below 400 nm (Fig. S12a), which is fitted to a Gaussian function resulting in three enhanced peaks (Fig. S12b). The ultra-high IPCE value activated by high-energy photons (blue line, Fig. 4d) is magnified by approximately 400%. A comparable enhancement is also attained in the second specimen, where the increase occurs at 350 nm (Fig. 4e). Between them (Fig. 4d and 4e), the shift of the enhancement peak is obvious, due to the difference of maximum electric field varied by plasmon resonances, similar to the shift of absorption resonance peaks (the insets in Fig. 4d and 4e). The offset between the enhanced peaks is also obtained in the Ti foil and Ni-coated Ti foil with annealing (Fig. S13) with cut-off edges at 350 nm (Fig. 4f), strongly indicating that the photons directly excited charge carriers through the surface TiO_2 generating the photocurrent. The coating of Ni was used to protect the surface from corrosion[39,40]. The result suggests that the OER activity is mainly caused by the hole carriers that are instantly excited by high energetic photons. In

addition, compared to the Ti foil without Ni (Fig. 4f), the achieved ultra-high conversion efficiencies (Fig. 4d and 4e), benefiting from the introduction of gradient-based dielectric, disclose that the direct photonic transition is enhanced by the localized electromagnetic field. This can be explained by the mechanism of plasmon-enhanced photonic energy transfer[11]. The absorption edge of TiO_{2-x} at 350 nm spectrally overlaps with the amplified near-field band, resulting in an increased light absorption that promoted the photonic transitions.

After deposition of a 2-nm thin film Ni (Fig. S14) followed by annealing, we investigated the energy transfer process in the second specimen Ti/TiO_{2-x} (Fig. S15). The derived IPCE spectrum highlights two distinct regions but has opposite polarities (Fig. 5a): one peak is at 360 nm, and the other negative peak is at 500 nm. The peak at 360 nm with a rational offset fits the enhancement profile but has a lower amplitude compared to the specimen without the Ni-coating (Fig. 4e). The adverse enhancement peak indicates the proton reduction reactions were activated under the light irradiation. Moreover, the IPCE curve faithfully follows the plasmon resonance absorption spectrum in the visible light region (Fig. 5b). This match confirms that the resonant absorption band obtained in the experimental absorption spectra originates from the excitation of SPRs. Further, the reduction reactions are driven through the hot electron injection mechanism[11,41], so that the Ti/TiO_{2-x} can utilize the plasmonic energy of visible light below the absorption band edge of TiO_{2-x}. Therefore, the plasmonic Ti/TiO_{2-x} possesses two distinct mechanisms, one is the enhanced photonic energy transfer of ultra-violet light by localized electric field, and the other is hot electron generation by plasmonic energy of visible light.

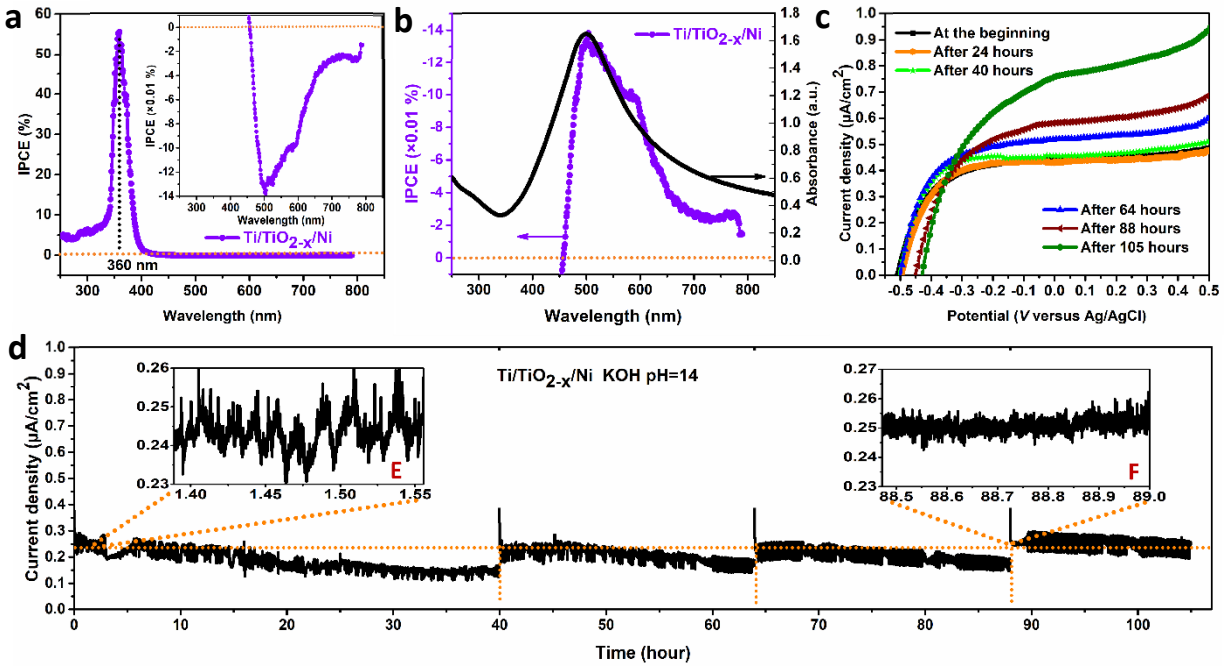

Fig. 5. Photoelectrochemical performance of the 2-nm Ni-coated Ti/TiO_{2-x}. (a) IPCE spectrum; the inset is the IPCE data within the negative range of the Y-axis. (b) Same as the inset in (a) but showing with data of y-axis in reverse (blue line). (c) Linear sweep voltammograms of the Ti/TiO_{2-x}/Ni taken at the different time points in order, 0 (at the beginning before the test), 24, 40, 64, 88 and 105 hours, respectively. All voltammograms were taken at 10 mV/s with no iR compensation applied. (d) Current density as a function of time, under constant illumination and potential of 0.21 V (versus Ag/AgCl) for over 100 hours. Insets (E and F) show details of the current with vibration fluctuations caused by oxygen gas bubbles release. The KOH aqueous solution in the cell was replaced using a completely new solution at the time moments of **I**, **II** and **III**, respectively, but maintaining the same volume.

We then investigated the stability of the Ni-coated Ti/TiO_{2-x} as a photoanode in the environment of photo-electrochemical system. The anode maintains OER activity for over 100 hours (Fig. 5d) under the simulated solar light illumination, although cyclic voltammograms taken in the times show a slight change after 64 hours of a continuous test in aqueous KOH solution (Fig. 5c). The UV-Vis absorption spectra show no deviation in the resonance intensity of surface plasmons after 106 hours. A control third specimen of the Ti/TiO_{2-x} without coating Ni was measured under the identical conditions (Fig. S16a). Apparent degradation of the light absorbance intensity can be observed in the UV-Vis spectra (Fig. S16b) after ~25 hours. Clearly, the corrosion is suppressed to a large extent by coating Ni as a protection layer. As a result, the long-term and stable resonant plasmons and transfer of photonic to chemical energy are ultimately obtained.

To examine the origin of the charge carriers, we performed a density functional theory (DFT) based calculation of electronic

properties on a doped Ti model (Fig. S17). The density of states (DOS) predicts an initial energy distribution of the carriers over energy bands close to the Fermi Level (Fig. S17, a-c). Increment in the oxygen concentration leads to stronger hybridization in *s, p* and *d* orbitals close to the Fermi level, which could provide local interband and intraband transitions of the charge carriers[42,43]. Also, the gap between the O_{2p} and Ti_{3d} energy levels tends to decrease, which allows a higher possibility of interband transitions by high-energy photons[44]. After heavy doping (Fig. S17c), the energy gap between O_{2p} and Ti_{3d} orbitals shows an onset threshold ~3.54 eV (350 nm), which correlates to the enhancement peak at 350 nm in the IPCE spectra. Thus, the charge carriers could be generated from both the interband and intraband transitions by the localized electromagnetic field enhancement. The interband transitions dominate the top surface positions while the intraband transitions are mainly below the surface region.

With the generated charge carriers, the mechanism for the separation and transportation of charge carriers is understood through a proposed schematic (Fig. S18) of the SPRs of Ti metal intensely coupling with the gradient-based TiO_{2-x} dielectrics[45]. Their built-in band bending can suppress undesirable recombination process while allowing charge carriers at low energy states to cross and be collected [46,47]. The Ti/TiO_{2-x} holds a gradient profile of oxygen elements in the surface region of Ti (Fig. S18a), forming a slight band bending (Fig. S18b). Upon the excitation of SPRs, the enhanced local electric field forms a deeper band bending. This is in line with the photovoltage ~350 mV observed when subjected to the alkaline solution. The excited charge carriers tend to recombine, but the pulling force of built-in electric field promotes the electrons and holes to transfer, accumulate and inhabit in the opposite directions away from the Fermi Level (Fig. S18c). With appropriate thermodynamic potential, the hole carriers are beneficial to the reaction sites involved in the OER, while the hot electrons injected into the conduction band of titanium oxides participate in the HER.

Conclusion

In summary, a solar-driven plasmonic heterostructure Ti/TiO_{2-x} is fabricated via the diffusion doping process on earth-abundant Ti. The resonant plasmons of Ti intensely coupling with gradient-based TiO_{2-x} dielectric confines light to a resonant absorption band and exhibits enhanced local electric field and hot electron generation effects. The excitation and quality of the SPRs in Ti/TiO_{2-x} are adjustable in the visible light range by tuning the thermal doping parameters. The strong interaction between plasmonic Ti and gradient-based TiO_{2-x} dielectric enhances the conversion of solar energy to charge carriers through the plasmon-enhanced photonic energy transfer and the hot electron injection mechanisms. By adding a protective Ni thin film, a more robust plasmon resonances in Ti/TiO_{2-x} is achieved in chemical environment that maintains long-lasting plasmon-enhanced activity over 100 hours.

The gradient-based heterostructure Ti/TiO_{2-x} represents a conceptually different approach to excite the SPRs by visible light and extract the plasmonic energy, using a thermal doping process to construct an intense coupling of Ti metal and gradient-based TiO_{2-x} dielectric. The Ti-based plasmonic structure with gradient doping could act as a platform to provide strong plasmon resonances in the visible light range and contribute to the conversion and storage of solar energy for sustainable plasmon-enhanced catalysis.

Experimental

Materials, Fabrications and characterizations

Titanium foils (Ti foils, L: 20mm × W: 14mm × T: 0.5 mm, 99.99% purity) were cut out from Ti sheet, which was purchased from Baoji Titanium Industry Co., LTD. The Ti foils were cleaned by immersing the foils into the acetone rinsed by ultrasonic bath and subsequently dried in flowing nitrogen gas. Fabrication of the Ti/TiO_{2-x} consists of two steps. Micro- and nano- prisms on the surface of the Ti foil was first fabricated via wet etching in a diluted hydrofluoric acid solution, followed by a thermal diffusion doping in a tube furnace with a controlled oxygen gas flowing.

Scanning electron microscope images with energy-dispersive X-ray analysis (Hitachi SU 8230), interferometry maps (Wyko NT9100) and atomic force microscope images (AFM XE-200) were used to confirm the morphology, surface roughness, and surface micro-prisms, respectively. X-ray diffraction (XRD) patterns were collected on an X-ray diffractometer using Cu Kα radiation (λ = 1.5405 Å) in a range of 2-80° (EQUINOX 1000, Thermo Fisher Scientific). Light absorption properties were measured using a SHIMADZU, UV-2600 spectrophotometer equipped with an integrated sphere assembly using diffuse reflection method. $BaSO_4$ was used as a reference to calibrate all samples in the wavelength range of 250 - 800 nm with a slit width of 1 nm. Absorbance was obtained by logarithmically plotting the measured reflectance spectrum [$\log(1/R_\infty)$]. Dark-field optical scattering images were taken using the optical microscope Leica DM3 XL. Sputtering machine (Sputter AJA) was used to deposit 2-nm ultrathin film of Nickel on the top of samples, followed by the ultra-vacuum annealing at 400 °C for 5 hours. Sputtering process was also employed to deposit the planar Ti film (300 nm) on the planar Si substrate.

Photoelectrochemical activities of Ti/TiO_{2-x} before and after coating ultrathin Ni were carried out using a three-electrode configuration on an electrochemical workstation of Model 600E Series. The Ti/TiO_{2-x} was employed as a working electrode, Pt foil as the counter electrode and Ag/AgCl with saturated KCl solution as the reference electrode. All the potentials are reported with respect to the Ag/AgCl electrode in saturated potassium chloride electrolyte. 0.5 M Na_2SO_4, 1 M KOH and 1 M NaOH aqueous solutions were used as an electrolyte in their respective experiments. Before each measurement, the aqueous solutions were bubbled with N_2 for 20 min to remove dissolved gas. IR compensation was automatically carried out in real time during the measurement unless otherwise stated. The visible light source employed in the measurement was a 500 W Xeon lamp with AM 1.5G filter. In 1M KOH aqueous solution,

the Ti/TiO_{2-x} and Ni-coated Ti/TiO_{2-x} are all under the illumination of AM 1.5G full-spectrum solar light with a power density of 100 mW/cm^2. All the PEC measurements were performed by using at least three samples, and each sample was tested more than three times. The IPCE spectra were measured using the same AM 1.5G solar light source coupling with a monochromator (F/4.8; focal length: 300 mm), at a constant bias of 0.21 V vs. Ag/AgCl. The IPCE data is the arithmetic mean of three consecutive measurements. During the IPCE measurement, the power intensity of the Xeon lamp source was kept at 100 mW/cm$_2$. IPCE (λ) = 1 240 J / (λI_{light}), where J is the measured photocurrent density (μA/cm^2), λ is the wavelength of the incident monochromatic light (nm) and I_{light} is the measured light intensity (μW/cm^2) at the wavelength of λ[48]. DFT based calculation models and optimal parameters are included in the Electronic Supplementary Information.

FEFD calculations

Finite element frequency domain (FEFD) simulations were performed using the commercially available COMSOL RF module[49,50]. An approximated simulation model was constructed by using Ti metal foil as a substrate, and TiO_2 thin film with TiO_2 nanoparticles in an ambient air atmosphere on the substrate. The Ti and TiO_2 were modelled respectively using the full frequency-dependent dielectric functions. A uniform plane transverse electric (TE) - polarized electromagnetic wave was incident on the model. The optical constants for the materials, TiO_2 and Ti, were taken from references[51,52], respectively. Perfectly matched layers (PML) were used in all boundaries to absorb the outgoing waves and simulate an open space around the model. The local field and absorption enhancement were both computed to investigate the nature of the constructed model. For more details, please refer to the Numerical calculations in supplementary information (Fig. S5 - S10).

Conflicts of interest

The authors declare no competing interests.

Acknowledgements

This work was supported by the China Scholarship Council (CSC, Grant No. 201506930002), and the Norwegian Micro- and Nano-Fabrication Facility project (NorFab, project No. 245963/F50). We thank Z. Ramic, M. Tayyib, A. T. Thai Nguyen and B. K. Hønsvall at the department of microsystems, USN, for the assistance during the experiments. We thank K. Weibye at the department of Chemistry, University of Oslo, for the discussions on surface states of the heterostructure.

Electronic Supplementary Information

Electronic Supplementary Information is available from the Online Library or from the author.

Notes and references

1 U. Aslam, V. G. Rao, S. Chavez, S. Linic, *Nat. Catal.* 2018, **1**, 656.
2 C. Zhan, X.-J. Chen, J. Yi, J.-F. Li, D.-Y. Wu, Z.-Q. Tian, *Nat. Rev. Chem.* 2018, **2**, 216.
3 S. Linic, P. Christopher, D. B. Ingram, *Nat. Mater.* 2011, **10**, 911.
4 M. L. Brongersma, N. J. Halas, P. Nordlander, *Nat. Nanotechnol.* 2015, **10**, 25.
5 C. Clavero, *Nat. Photonics* 2014, **8**, 95.
6 X. Liu, J. Iocozzia, Y. Wang, X. Cui, Y. Chen, S. Zhao, Z. Li, Z. Lin, *Energy Environ. Sci.* 2017, **10**, 402.
7 S. Eustis, M. A. el-Sayed, *Chem. Soc. Rev.* 2006, **35**, 209.
8 R. Jiang, B. Li, C. Fang, J. Wang, *Adv. Mater.* 2014, **26**, 5274.
9 C. Jia, X. Li, N. Xin, Y. Gong, J. Guan, L. Meng, S. Meng, X. Guo, *Adv. Energy Mater.* 2016, **6**, 1600431.
10 N. Wu, *Nanoscale* 2018, **10**, 2679.
11 J. Li, S. K. Cushing, P. Zheng, F. Meng, D. Chu, N. Wu, *Nat. Commun.* 2013, **4**, 2651.
12 S. Kim, J. M. Kim, J. E. Park, J. M. Nam, *Adv. Mater.* 2018, **30**, e1704528.
13 I. Roger, M. A. Shipman, M. D. Symes, *Nature Reviews Chemistry* 2017, **1**, 0003.
14 J. H. Montoya, L. C. Seitz, P. Chakthranont, A. Vojvodic, T. F. Jaramillo, J. K. Norskov, *Nat. Mater.* 2016, **16**, 70.
15 A. Agrawal, S. H. Cho, O. Zandi, S. Ghosh, R. W. Johns, D. J. Milliron, *Chem. Rev.* 2018, **118**, 3121.
16 Y. Hsun Su, C.-Y. Hsu, C.-C. Chang, S.-L. Tu, Y.-H. Shen, *Appl. Phys. Lett.* 2013, **103**, 063703.
17 J. P. Zhao, M. Lu, Z. Y. Chen, J. W. Rabalais, *Appl. Phys. Lett.* 2002, **80**, 3626.
18 V. Jokanović, B. Čolović, M. Nenadović, A. Trajkovska Petkoska, M. Mitrić, B. Jokanović, I. Nasov, *Adv. Mater. Sci. Eng.* 2016, **2016**, 1.
19 V. Jokanović, B. Čolović, B. Jokanović, S. Stojadinović, A. Petkoska-Trajkovska, I. Nasov, *Zastita materijala* 2016, **57**, 225.
20 A. Fujishima, K. Honda, *Nature* 1972, **238**, 37.
21 M. Pelaez, N. T. Nolan, S. C. Pillai, M. K. Seery, P. Falaras, A. G. Kontos, P. S. M. Dunlop, J. W. J. Hamilton, J. A. Byrne, K. O'Shea, M. H. Entezari, D. D. Dionysiou, *Appl. Catal. B-Environ.* 2012, **125**, 331.
22 L. Gomathi Devi, R. Kavitha, *Appl. Surf. Sci.* 2016, **360**, 601.
23 V. A. Vlaskin, C. J. Barrows, C. S. Erickson, D. R. Gamelin, *J. Am. Chem. Soc.* 2013, **135**, 14380.
24 J. M. Luther, P. K. Jain, T. Ewers, A. P. Alivisatos, *Nature materials* 2011, **10**, 361.
25 J. J.W. ROGERS, K.L. ERICKSON, D.N. BELTON, *Appl. Surf. Sci.* 1988, **35**, 16.
26 Y. Horio, Y. Hara, Y. Yamamoto, Y. Morimoto, T. Naitoh, *Jpn. J. Appl. Phy.* 2012, **51**, 015604.
27 C. Cheng, G. Liu, K. Du, G. Li, W. Zhang, S. Sanna, Y. Chen, N. Pryds, K. Wang, *Appl. Catal. B-Environ.* 2018, **237**, 416.
28 S. M. Wu, X. L. Liu, X. L. Lian, G. Tian, C. Janiak, Y. X. Zhang, Y. Lu, H. Z. Yu, J. Hu, H. Wei, H. Zhao, G. G. Chang, G. Van Tendeloo, L. Y. Wang, X. Y. Yang, B. L. Su, *Adv. Mater.* 2018, **30**, e1802173.
29 Y. Liu, R. Cheng, L. Liao, H. Zhou, J. Bai, G. Liu, L. Liu, Y. Huang, X. Duan, *Nat. Commun.* 2011, **2**, 579.
30 V. N. Kuznetsov, N. Serpone, *J. Phys. Chem. B* 2006, **110**, 25203.
31 M. A. Mahmoud, M. Chamanzar, A. Adibi, M. A. El-Sayed, *J. Am. Chem. Soc.* 2012, **134**, 6434.
32 P. Mulvaney, *Langmuir* 1996, **12**, 788.
33 M. Ian Lapsley, A. Shahravan, Q. Hao, B. Krishna Juluri, S. Giardinelli, M. Lu, Y. Zhao, I. K. Chiang, T. Matsoukas, T. Jun Huang, *Appl. Phys. Lett.* 2012, **100**, 101903.

34 T. Hutter, F. M. Huang, S. R. Elliott, S. Mahajan, *J. Phys. Chem. C* 2013, **117**, 7784.
35 F. Le Formal, S. R. Pendlebury, M. Cornuz, S. D. Tilley, M. Gratzel, J. R. Durrant, *J. Am. Chem. Soc.* 2014, **136**, 2564.
36 J. Kamimura, P. Bogdanoff, M. Ramsteiner, P. Corfdir, F. Feix, L. Geelhaar, H. Riechert, *Nano Lett.* 2017, **17**, 1529.
37 J. S. DuChene, G. Tagliabue, A. J. Welch, W. H. Cheng, H. A. Atwater, *Nano Lett.* 2018, **18**, 2545.
38 L. M. Peter, *J. Solid State Electrochem.* 2012, **17**, 315.
39 M. J. Kenney, M. Gong, Y. Li, J. Z. Wu, J. Feng, M. Lanza, H. Dai, *Science* 2013, **342**, 836.
40 Y. Yang, Y. Ling, G. Wang, T. Liu, F. Wang, T. Zhai, Y. Tong, Y. Li, *Nano Lett.* 2015, **15**, 7051.
41 S. K. Cushing, J. Li, F. Meng, T. R. Senty, S. Suri, M. Zhi, M. Li, A. D. Bristow, N. Wu, *J. Am. Chem. Soc.* 2012, **134**, 15033.
42 R. Sundararaman, P. Narang, A. S. Jermyn, W. A. Goddard, H. A. Atwater, *Nat. Commun.* 2014, **5**, 5788.
43 P. Narang, R. Sundararaman, H. A. Atwater, *Nanophotonics* 2016, **5**.
44 Y. Kim, J. G. Smith, P. K. Jain, *Nat. Chem.* 2018, **10**,763.
45 C.-S. Jiang, F. S. Hasoon, H. R. Moutinho, H. A. Al-Thani, M. J. Romero, M. M. Al-Jassim, *Appl. Phys. Lett.* 2003, **82**, 127.
46 F. F. Abdi, L. Han, A. H. Smets, M. Zeman, B. Dam, R. van de Krol, *Nat. Commun.* 2013, **4**, 2195.
47 N. Wang, M. Liu, H. Tan, J. Liang, Q. Zhang, C. Wei, Y. Zhao, E. H. Sargent, X. Zhang, *Small* 2017, **13**.
48 Z. Yi, J. Ye, N. Kikugawa, T. Kako, S. Ouyang, H. Stuart-Williams, H. Yang, J. Cao, W. Luo, Z. Li, Y. Liu, R. L. Withers, *Nat. Mater.* 2010, **9**, 559.
49 R. A. Pala, J. White, E. Barnard, J. Liu, M. L. Brongersma, *Adv. Mater.* 2009, **21**, 3504.
50 R. Asapu, R. G. Ciocarlan, N. Claes, N. Blommaerts, M. Minjauw, T. Ahmad, J. Dendooven, P. Cool, S. Bals, S. Denys, C. Detavernier, S. Lenaerts, S. W. Verbruggen, *ACS Appl. Mater. Inter.* 2017, **9**, 41577.
51 T. Siefke, S. Kroker, K. Pfeiffer, O. Puffky, K. Dietrich, D. Franta, I. Ohlídal, A. Szeghalmi, E.-B. Kley, A. Tünnermann, *Adv. Opt. Mater.* 2016, **4**, 1780.
52 W. S. M. Werner, K. Glantschnig, C. Ambrosch-Draxl, *J. Phys. Chem. Ref. Data* 2009, **38**, 1013.